



Double hysteresis loop in synchronization transitions of multiplex networks: The role of frequency arrangements and frustration

Ali Seif, Mina Zarei *

Institute of Advanced Studies in Basic Sciences (IASBS), Department of Physics, Zanjan, 45137-66731, Iran

ARTICLE INFO

Dataset link: [https://github.com/Articles-data/
Frequency-Arrangement](https://github.com/Articles-data/Frequency-Arrangement)

Keywords:

Explosive synchronization
Multiplex networks
Frustration
Phase-amplitude coupling

ABSTRACT

This study explores the dynamics of two-layer multiplex networks, focusing on how frequency distributions among mirror nodes influence phase transitions and synchronization across layers. We present a Regular frequency assignment model for duplex networks, where the layers are fully connected and share identical sets of natural frequencies. By adjusting the sizes of sections where nodes exhibit positive, zero, or negative frequency differences relative to their mirrored equivalents in another layer, we can effectively control the average frequency discrepancy between the layers. We compared the dynamics of this structured model to those with randomly distributed frequencies, keeping a constant average frequency difference between the layers and introducing a phase lag in the interlayer interaction terms. This comparison highlighted distinct behaviors, including double hysteresis loops in the synchronization phase transition and standing waves for intralayer coupling at the locations of the hysteresis loops, where the waves are composed of different interacting frequencies.

0. Introduction

Multilayer networks have attracted considerable interest due to their prevalence in complex systems. Many real-world networks, including social, technological, and biological structures, can be represented as multilayer systems with different interactions across layers [1–6]. The brain serves as an excellent example of a multilayer network, with distinct layers representing various types of connectivity, such as structural, functional, and effective connections [7–9]. Furthermore, the brain's multilayer framework encompasses a range of interactions between neurons, such as chemical and electrical synapses, along with volume transmission [10]. Different brain regions also communicate across diverse frequency bands, creating communication layers that facilitate various cognitive functions [11,12]. Thus, examining these multilayer structures can provide valuable insights into the dynamics and functionality of the brain.

Synchronization is a fascinating phenomenon observed in various systems, including ecological, biological, and technological networks [13,14]. Researchers have studied the synchronization of networks made up of neurons and phase oscillators using diverse models [15–18]. The Kuramoto model serves as a foundational framework for examining synchronization in oscillatory systems, providing insights into how oscillators synchronize based on their coupling strengths and natural frequencies [19]. This model has been extended to incorporate realistic features of real-world systems, such as time delays [20,21],

inertia [22,23], phase lags [24–26], and interlayer interactions [27–37].

A key area of research centers on explosive synchronization, which involves a sudden shift to synchronized behavior. This phenomenon is crucial for numerous applications and has been linked to events such as cascading failures in power grids [38], coupled chemo-mechanical systems [39], and chronic pain or epileptic seizures in the brain [40,41]. Previous studies have explored the characteristics and structures that contribute to explosive synchronization in complex networks [42–44]. For example, in single-layer networks, a correlation between node degree and natural frequency has been shown to promote explosive synchronization [45,46]. However, this correlation is not necessary; explosive synchronization can also occur in adaptive networks that do not exhibit such a relationship [28]. Additionally, abrupt synchronization transitions have been noted in fully connected networks with bimodal natural frequency distributions [47]. Furthermore, explosive synchronization has been observed in multiplex networks [27–32,48–53].

In this study, we explore how frequency arrangements in duplex networks influence their dynamics. We find that not only does the average frequency mismatch between mirror nodes impact the dynamics, but their specific configuration also plays a significant role. Previous research has demonstrated that explosive synchronization can arise from

* Corresponding author.

E-mail address: mina.zarei@iasbs.ac.ir (M. Zarei).

random frequency mismatches between mirror nodes across different layers, especially when interlayer interactions experience frustrations around $\frac{\pi}{2}$ [31]. Introducing frustrations or phase lags in the Kuramoto model's interaction terms typically alters the phase response curves of the oscillators, which subsequently affects the overall network dynamics [16,54,55]. Additionally, frustrations interact in complex ways with the natural frequencies of nodes during synchronization [56,57].

We propose a model of regular frequency arrangements that illustrates irreversibility and memory in the synchronization transition curves of duplex networks, even in the absence of phase lag in interlayer interactions. By introducing frustrations of approximately $\frac{\pi}{2}$ in the interlayer interaction terms, we observe transition curves featuring double hysteresis loops. We observe periodic synchrony within the area of intralayer couplings, where hysteresis loops emerge. The observed waves consist of multiple frequency bands that interact with each other. Specifically, the amplitude of faster waves modulates the phase of slower waves, illustrating a dependence between these frequency bands. We quantify the interaction between phase and amplitude through phase-amplitude coupling, a measure used for brain waves that demonstrates how different frequency bands interact across various time scales. This interaction facilitates complex cognitive processes and enhances efficient information processing [58–60].

The paper is organized as follows: The first section offers a comprehensive overview of the structure and dynamical models, detailing the formulas and metrics utilized in our study. **results** presents the numerical findings, emphasizing the synchronization transition curve of duplex networks, both with and without frustration in interlayer connections. We also investigate the periodic behavior noted in specific intralayer links and the interactions between the various oscillatory rhythms of the observed waves. Finally, the **discussion** section highlights our main conclusions.

1. Material and methods

1.1. Network topology and dynamics

Our implementation involves the utilization of a duplex network, a multiplex system consisting of two interconnected layers with all-to-all connectivity. We represent the nodes in each layer using Kuramoto oscillators as our chosen model. These oscillators serve as the nodes within each layer and capture their dynamic behavior. **Mirror nodes** are pairs of nodes that represent the same entity across different layers of a multiplex network. In our model, these nodes are connected through an interlayer coupling mechanism that influences the synchronization and dynamics of the Kuramoto oscillators, enabling information exchange across the network's layers. A visual representation of a duplex network can be found in Fig. 1. The interaction between mirror nodes across different layers is illustrated using dashed lines.

The original Kuramoto model was developed for all-to-all interactions [19]; however, it has been adapted for a variety of network structures over time [15]. In this study, we utilize an extended version of the Kuramoto model to investigate the dynamics of a duplex network comprising two interconnected layers [31]. The phase evolution of the i^{th} node in layer I and its mirror in layer II is described by the following equations:

$$\dot{\theta}_i^I = \omega_i^I + \frac{\sigma}{N} \sum_{j=1}^N \sin(\theta_j^I - \theta_i^I) + \lambda \sin(\theta_i^{II} - \theta_i^I + \alpha), \quad (1)$$

$$\dot{\theta}_i^{II} = \omega_i^{II} + \frac{\sigma}{N} \sum_{j=1}^N \sin(\theta_j^{II} - \theta_i^{II}) + \lambda \sin(\theta_i^I - \theta_i^{II} + \alpha). \quad (1)$$

where $\theta_i^{I(II)}$ indicates the phase of the i^{th} node in layer I(II), and $\omega_i^{I(II)}$ represents the natural frequency of the i^{th} node in layer I(II). The intralayer coupling strength, σ , is identical for both layers, and the interlayer coupling strength is denoted by λ . The variable N represents

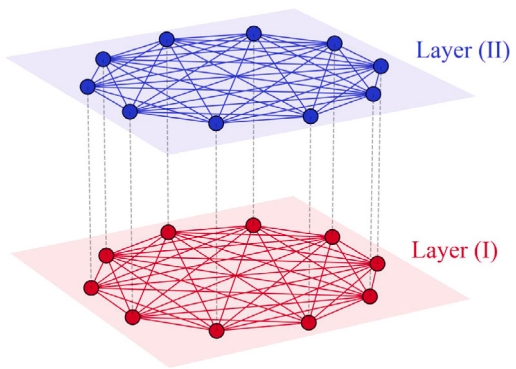


Fig. 1. Schematic representation of a duplex network with fully connected layers. Dashed lines indicate interlayer couplings between mirror nodes.

the total number of nodes in each layer of the duplex network. A frustration parameter, represented as α , is incorporated into the interlayer interaction terms to account for phase lags between corresponding mirror nodes, thereby influencing their synchronization dynamics.

To quantify the degree of synchronization within each layer, the synchronization order parameter is defined as follows:

$$r^{I(II)} e^{i\psi^{I(II)}} = \frac{1}{N} \sum_{j=1}^N e^{i\theta_j^{I(II)}}. \quad (2)$$

The synchronization order parameter, represented as $r^{I(II)}$, ranges from 0 to 1. A value of 1 reflects complete synchronization in the respective layer, where all nodes are in phase, whereas a value of 0 indicates total asynchrony. $\psi^{I(II)}$ represents the collective phase value, which can range between 0 and 2π . The long-term average of the synchronization order parameter $r^{I(II)}$, denoted as $R^{I(II)}$, provides insights into the overall level of synchronization in the stationary state within each layer. In our simulation, we compute the average $R^{I(II)}$ over the last 80% of the simulation duration, which reflects the period when the system has reached its stationary state.

To investigate synchrony within specific subsets of nodes in each layer, we define a local order parameter $R_g(t)$, where g denotes different groups of oscillators. This parameter quantifies synchrony among selected oscillators, providing insights into localized behaviors that may vary from the overall dynamics of the network. The calculation method is as follows:

$$R_g(t) = \frac{1}{N_g} \left| \sum_j e^{i\theta_j(t)} \right|, \quad (3)$$

here, N_g represents the number of nodes in the selected group, and the sum is computed over these nodes.

To quantitatively assess the instantaneous phase similarity between the phases of all node pairs at a given time, we define the phase similarity matrix for each layer, denoted as $S^{I(II)}(t)$, along with the phase similarity of mirror nodes, represented by $S_{M_i}(t)$, as follows:

$$S_{ij}^{I(II)}(t) = \cos(\theta_i^{I(II)}(t) - \theta_j^{I(II)}(t)), \quad (4a)$$

$$S_{M_i}(t) = \cos(\theta_i^{II}(t) - \theta_i^I(t)). \quad (4b)$$

The phase similarity indices take values in the range $[-1, 1]$, where 1 signifies an in-phase relationship, and -1 indicates an anti-phase relationship between a specified pair of nodes at a given time point.

In our simulation, we consider $N = 1000$. The initial phases of the oscillators are randomly sampled from a uniform distribution within the range $-\pi < \theta_i^{I(II)} \leq \pi$. To achieve the results, we numerically solve Equations (1) employing the fourth-order Runge–Kutta method, with a time step of $dt = 0.01$. Each simulation is run for a total of 40,000 steps.

1.2. Frequency arrangement models for mirror nodes in duplex networks

We have outlined the structure and dynamical model used in our study, along with methods for quantifying emergent behavior. Our main objective is to investigate how frequency arrangements among mirror nodes influence the collective behavior of the duplex network. To achieve this, we employ two different models: the **Random model** and the **Regular model**. The results related to the random model are reproductions of the findings from paper by Kumar et al. [31], which are presented for comparison with the Regular model we introduce. To ensure comparability, the average natural frequency differences between mirror nodes in the two layers of both models can be maintained, even though frequency patterns may vary at a microscopic level. In the following, we will describe two models in detail and explain their differences.

The natural frequencies in each layer are chosen as evenly spaced values ranging from -0.5 to 0.5 . In this paper, for both models, the natural frequencies of the nodes in layer I are organized in ascending order, with node $i = 1$ assigned the minimum frequency of -0.5 and node $i = N$ assigned the maximum frequency of 0.5 . The following formula is used to establish these frequencies in the layer I:

$$\omega_i^I = -0.5 + \frac{i-1}{N-1}. \quad (5)$$

The set of natural frequencies in the layer II is identical to that in the layer I, differing only in the arrangement of these frequencies among the nodes within this layer. This variation in configuration can lead to differences in the frequencies of mirror nodes, meaning that ω_i^{II} may not be equal to ω_i^I . As a result, there can be a non-zero average frequency difference between mirror nodes in the two layers. The average differences in natural frequencies between mirror nodes can be quantified as follows:

$$\Delta\omega = \frac{\sum_{i=1}^N |\delta\omega_i|}{2 \sum_{i=1}^N |\omega_i^I|}, \quad (6)$$

where $\delta\omega_i = \omega_i^{II} - \omega_i^I$; consequently, the value of $\Delta\omega$ ranges from 0 to 1. When mirror nodes have identical frequencies ($\omega_i^I = \omega_i^{II}$), $\Delta\omega$ is 0. In contrast, when mirror nodes have the maximum frequency difference ($\omega_i^I = -\omega_i^{II}$), $\Delta\omega$ is 1. As previously noted, the nodes in layer I are organized in ascending order according to their natural frequencies. Changes in the arrangement of node frequencies in layer II result in notable frequency discrepancies between the two layers, which can be quantified by the parameter $\Delta\omega$. The distinction between the Random and Regular models is based on the arrangement of frequencies in layer II, which is specifically configured to achieve a desired $\Delta\omega$.

To implement the Random model for achieving a specific target value of $\Delta\omega$, the process begins by organizing the second layer in a sorted order, identical to that of the first layer, where $\Delta\omega = 0$. Following this initial arrangement, two nodes are randomly selected from the second layer, and their natural frequencies are swapped. If this swap results in a $\Delta\omega$ that is closer to the desired target, the change is accepted. Conversely, if the result does not bring the $\Delta\omega$ closer to the target, the frequencies are reverted to their previous configuration. This iterative adjustment continues until the intended $\Delta\omega$ value is successfully achieved.

To achieve a targeted $\Delta\omega$ value using the Regular algorithm, we begin by organizing the nodes in both layers in ascending order based on their natural frequencies, initially setting $\Delta\omega$ to zero. In this study, we refer to pairs of nodes within each layer, labeled i and $N+1-i$, as **counterpart nodes**. In each step S , we select two counterpart nodes from layer II that demonstrate the greatest frequency differences with their corresponding mirror nodes in layer I and have not been previously selected, then swap their frequencies, specifically $\omega_S^{II} \leftrightarrow \omega_{N+1-S}^{II}$. If the resultant $\Delta\omega$ is equal to or less than the desired value, we retain the change. Conversely, if the deviation exceeds the intended $\Delta\omega$,

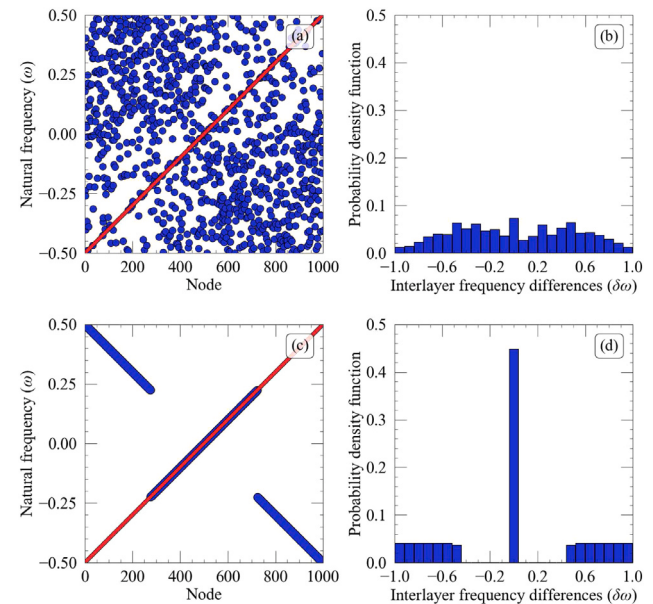


Fig. 2. A visual representation showing the differences between Random and Regular models for frequency arrangement in a duplex network, both with $\Delta\omega = 0.8$. (Left column) Red dots illustrate the natural frequencies of the nodes in layer I, which are arranged in ascending order. Blue dots illustrate the natural frequencies of the nodes in layer II for the (a) Random model and (c) Regular model. Panel (c) identifies three distinct groups of nodes with positive, zero, and negative frequency differences ($\delta\omega_i$), referred to as the left, middle, and right parts, respectively. (Right column) The distribution function representing the magnitude of frequency differences between the mirror nodes, for the (b) Random model and (d) Regular model.

we revert the nodes to their original frequencies. This iterative process continues until we successfully achieve the specified $\Delta\omega$ value.

The visual representation in Fig. 2 demonstrates how both Random and Regular algorithms are applied to generate distinct frequency arrangements while maintaining a constant $\Delta\omega$ value of 0.8. As previously mentioned, the network consists of two fully connected layers, forming a duplex structure. In layer I, nodes are arranged in ascending order of their frequencies, corresponding to the red-colored secondary diagonal of the squares in Fig. 2a,c. In the Random model, the frequencies of nodes in layer II are randomly assigned, leading to an almost uniform distribution of frequency differences between corresponding mirror nodes (Fig. 2a,b). In contrast, in the Regular model, we can observe the presence of three distinct sets of nodes, which we will refer to as **left**, **middle**, and **right** hereafter. The nodes in the middle part exhibit zero frequency differences with their mirror nodes in layer I ($\delta\omega_i = \omega_i^{II} - \omega_i^I = 0$), while the nodes in the left and right parts display positive and negative frequency differences, respectively (see Fig. 2c). This indicates a multimodal distribution of frequency discrepancies, as shown in Fig. 2d.

1.3. Phase-amplitude coupling analysis

Neural oscillations are synchronized rhythmic patterns of electrical activity generated by neurons in the brain. **Phase-Amplitude Coupling (PAC)** is an important concept in neuroscience, employed to explore how the phase of low-frequency neural oscillations relates to the amplitude of high-frequency brain waves [61]. This establishes a framework for organizing and integrating neural information. It is fascinating how low-frequency oscillations can provide a timing mechanism for integrating the more detailed information carried by high-frequency oscillations. This coordination is essential for various cognitive processes, including attention, memory formation, and sensory perception [58–60]. Multiple methods have been developed to measure PAC [62–65]. In this paper, we will focus on two of these methods.

The modulation index of the **Phase-Locking Value (PLV)** serves as a key metric for evaluating the coordination between the phase of a **Low-Frequency Oscillation (LFO)** and the amplitude envelope of a **High-Frequency Oscillation (HFO)** [66]. To compute the PLV, the phase time series of the low-frequency oscillation (ϕ_l) and the amplitude envelope of the high-frequency oscillation (A_h) are first extracted from the original signal using the Hilbert transform. Once the extraction is complete, the modulation index is analyzed to evaluate the degree of synchronization between the LFO and HFO, employing the following formula:

$$PLV = \frac{\left| \sum_{j=1}^T e^{i(\phi_l(j) - \phi_{A_h}(j))} \right|}{T}. \quad (7)$$

The summation over all T time points aggregates the complex values corresponding to the phase differences at each time point. The normalized absolute value of the summed complex number gives a number between 0 and 1. A PLV of 1 indicates perfect phase synchronization, meaning that the phase relationship between two signals is consistent across all time points. On the other hand, a PLV of 0 suggests no consistent phase relationship between the signals. Essentially, high PLV values indicate a correlation between the phase of low-frequency oscillations (LFOs) and the amplitude of high-frequency oscillations (HFOs), while low values suggest a lack of correlation.

Visualization of correlation can be achieved by plotting unit-length vectors, $e^{i(\phi_l(j) - \phi_{A_h}(j))}$ on a polar plane at various time points. Each vector's angle represents the phase difference between the signals. The degree of correlation is represented by averaging these unit vectors. The magnitude of the resulting vector indicates the PLV. Its direction reflects the phase of the low-frequency signal at which the amplitude of the high-frequency signal is amplified.

The **Mean-Vector Length (MVL)** modulation index serves as an secondary metric for assessing the synchronization between the phase of LFOs and the amplitude of HFOs [67]. To calculate this index, the phases of the LFO (ϕ_l) and the amplitude envelope of the HFO (A_h) are obtained from frequency-filtered signals using the Hilbert transform. Subsequently, the phase angles are grouped into bins labeled by the index j , and the average amplitude of the HFO within each phase bin of the LFO, denoted as $\langle A_h \rangle_{\phi_l(j)}$, is computed and normalized according to the following formula:

$$P_{(j)} = \frac{\langle A_h \rangle_{\phi_l(j)}}{\sum_{k=1}^B \langle A_h \rangle_{\phi_l(k)}}, \quad (8)$$

where B represents the total count of phase bins. The Shannon entropy, obtained from the histogram mentioned previously as, $H(p) = -\sum_{j=1}^B P_{(j)} \log P_{(j)}$, provides valuable insights into the correlation between phase and amplitude. This information contributes to the calculation of the modulation index of MVL through the following formula:

$$MVL = 1 - \frac{H(p)}{\log B}. \quad (9)$$

The modulation index varies between 0 and 1, with higher values signaling more pronounced phase–amplitude coupling. The graph of $P(j)$ against j also visually illustrates the relationship between phase and amplitude.

Through the calculation of PLV or MVL and plotting their corresponding results, one can determine the presence of phase–amplitude coupling between different frequency bands of a signal.

2. Results

Our primary goal is to explore how patterns of frequency arrangements, which create frequency discrepancies between the two layers, influence the dynamics of a duplex network with frustrated interlayer interactions. Fig. 3 depicts the transition from incoherent to coherent states in layer II of a duplex network, driven by intralayer coupling. The first row illustrates the phase transition for the Random model, whereas

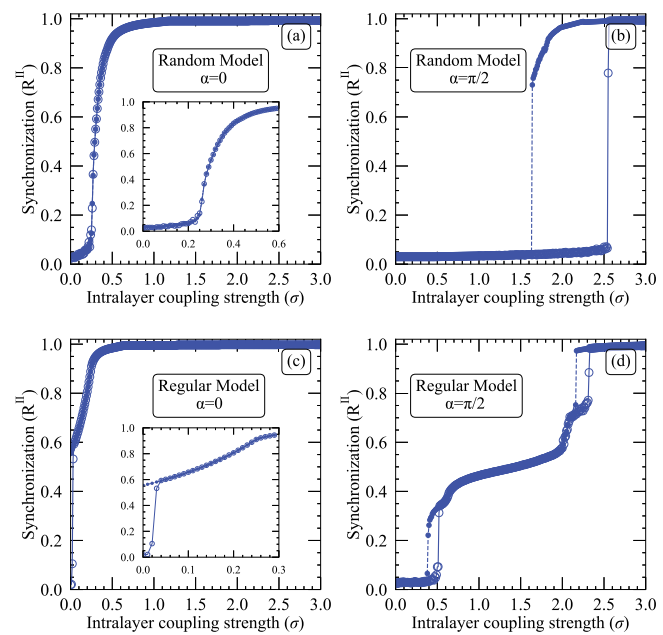


Fig. 3. Phase transitions from incoherent to coherent states occur as the intralayer coupling strength varies in a duplex network, utilizing two different frequency arrangement models. The results in the top row are associated with the Random model, while those in the bottom row pertain to the Regular model. The left column corresponds to $\alpha = 0$, and the right column corresponds to $\alpha = \frac{\pi}{2}$. Solid lines with unfilled points indicate forward transitions, while dashed lines with filled points represent backward transitions. The parameters used are $\Delta\omega = 0.8$ and $\lambda = 10$.

the second row presents the results for the Regular model. It is worth noting that the phase transition curves for both layers are quite similar, but we only present the results for the second layer here.

In the Random model, the phase transition at $\alpha = 0$ is continuous, while at $\alpha = \frac{\pi}{2}$, it appears discontinuous, exhibiting a hysteresis loop. This behavior aligns with the earlier findings of Anil Kumar et al. who demonstrated that the interaction between frequency discrepancies in the two layers and the frustration parameter near $\frac{\pi}{2}$ can lead to explosive synchronization [31].

In the Regular model with $\alpha = 0$, the transition curve is predominantly reversible across most intralayer couplings. However, at very low coupling values, a narrow hysteresis loop appears, indicating some irreversibility associated with the synchronization of the left and right sections. Beyond this range, the middle part synchronizes reversibly (see first row of the supplementary Fig. SF1 and Fig. SF2). This phenomenon likely results from the multimodal distribution of frequency discrepancies. In the backward curve, the nodes in both the right and left sections remain synchronized with zero frequency, even at $\sigma = 0$. The supplementary video, SV1, illustrates the time evolution of the order parameter for the left, right, and middle sections, along with the phase similarity matrix at $\sigma = 0$. It clearly shows that the nodes in the left and right sections are synchronized at the average frequency, while the nodes in the middle section are not phase-locked.

When a frustration of $\alpha = \frac{\pi}{2}$ is applied to the Regular model, with $\Delta\omega = 0.8$, a double hysteresis loop emerges in the phase transition curve. This indicates that the transition from incoherence to coherence occurs in two stages, each defined by distinct transition couplings, σ_T^1 and σ_T^2 . The first transition takes place at a low intralayer coupling of $\sigma_T^1 = 0.5$, and the second occurs at $\sigma_T^2 = 2.3$ along the forward curve. Fig. 3b demonstrates that the Random model exhibits a single bistable region between incoherence and coherence at high coupling strengths. In contrast, the Regular model displays a bistable regime between asynchrony and partial synchronization at low coupling strengths, along with another regime transitioning from partial

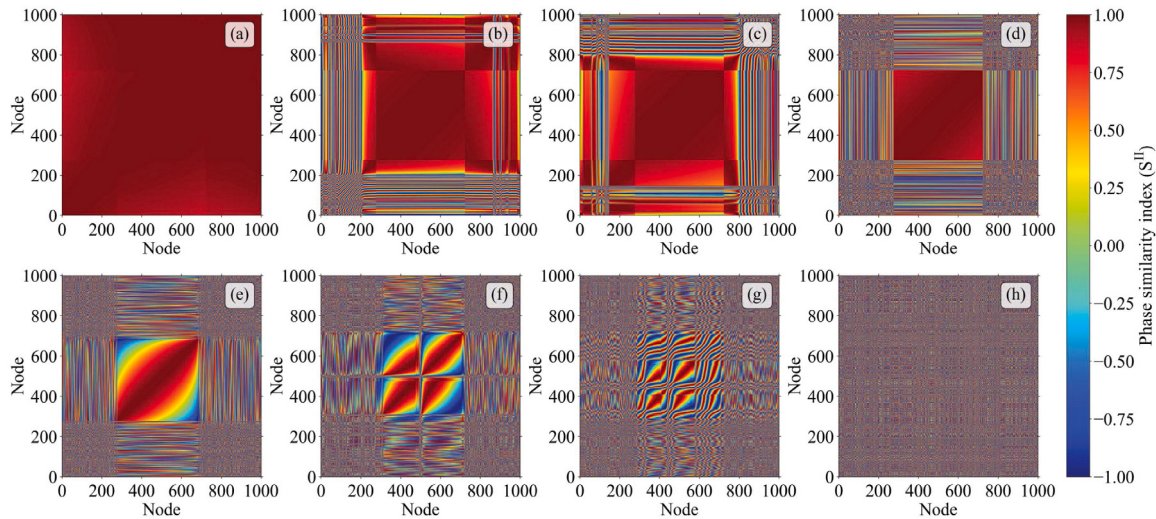


Fig. 4. The instantaneous phase similarity matrices for layer II at different intralayer coupling strengths in the backward paths are presented. The figures are arranged from top to bottom right, corresponding to intralayer coupling strengths (σ) of 2.71, 2.14, 2.13, 1.61, 0.60, 0.39, 0.38, and 0.09, respectively. This analysis used the Regular model for frequency assignment and the same parameters as those in Fig. 3d.

to complete synchronization at high coupling strengths. While the Random model remains asynchronous at low intralayer couplings, the Regular model can achieve partial synchronization. It is important to note that in both the Random and Regular models, all parameters remain constant, including $\Delta\omega = 0.8$, which quantifies the average frequency discrepancy between mirror nodes in the two layers. The key distinction that explains the observed variations in transition curves lies in the specific patterns of frequency arrangements that create discrepancies between the layers.

An analysis of the transition curves for the middle, left, and right sections reveals that the first observed hysteresis loop in Fig. 3d corresponds to the synchronization of the middle section, while the second loop is associated with the synchronization of the left and right sections, as illustrated in the second row of the supplementary Fig. SF1. This result contrasts with the case of $\alpha = 0$, where the left and right sections synchronize at low intralayer couplings, while the middle section only starts to synchronize at higher couplings. In other words, positioning the frustration close to $\frac{\pi}{2}$ causes the arrangement of coupling configurations that synchronize the three different parts — left, middle, and right — to change along the transition curves (see supplementary Fig. SF1).

As previously mentioned, earlier studies have shown that frequency discrepancies between layers in duplex networks with frustrated interlayer interactions can lead to explosive synchronization [31]. However, in the Regular model, the middle section — where the frequency discrepancy between mirror nodes is zero — also exhibits explosive synchronization (see Fig. 3d). This is probably due to the complex interaction between the multimodal distribution of frequency discrepancies and frustration.

To gain a comprehensive understanding of the transition depicted in Fig. 3d, we have plotted the instantaneous phase similarity matrix, S , for various values of the intralayer couplings in Fig. 4, focusing on the backward path in layer II. In fact, since the level of synchronization is higher on the backward path, we will have a better view of the details. In Fig. 4, red points indicate in-phase synchronization between the two nodes ($S_{ij}(t) = 1$), while blue points represent anti-phase synchronization ($S_{ij}(t) = -1$).

Fig. 4 illustrate the changes in the phase similarity matrix patterns as the intralayer couplings are decreased, highlighting the transition from coherent to incoherent states. Fig. 4a shows that when there is strong intralayer coupling, such as $\sigma = 2.71$, all nodes in layer II are nearly synchronized. Fig. 4b,c demonstrate that as the coupling is reduced to the region of the second hysteresis loop, the network exits the synchronized state; either the left part (Fig. 4b) or the right part

(Fig. 4c) loses coherence, while the remaining parts stay synchronized. Then, as the intralayer coupling strength decreases further, for example to $\sigma = 1.61$, only the nodes in the middle part — those have the same natural frequencies as their mirror nodes in the other layer — continue to synchronize (Fig. 4d). As the coupling strength is reduced even more, the middle part also transitions out of the synchronized state (Fig. 4e). With the continuation of the declining process, in the first hysteresis loop, the nodes in the middle part create synchronized clusters of those with similar natural frequencies (Fig. 4f,g). The less intralayer coupling there is, the more clusters there will emerge. Ultimately, with minimal intralayer coupling, we observe an incoherent state (Fig. 4h). In summary, the figure demonstrates that the first hysteresis loop is associated with the transition of the middle component to a synchronized state. In contrast, the second hysteresis loop corresponds to the synchronization of the left and right parts with the middle section. This finding aligns with the result shown in supplementary Fig. SF1. It is important to note that the phase similarity matrices shown are plotted at a single time point within stationary states. The question that arises is: how do the dynamics behave during stationary states? In continuation, we will concentrate on the dynamics within the region of the hysteresis loops.

Fig. 5a depicts the time evolution of the synchronization order parameter for the left, middle, and right parts of the network, as well as for the entire network, with the intralayer coupling set to $\sigma = 0.39$ within the first hysteresis loop. It can be observed that the left and right parts are not synchronized. Moreover, the entire network displays oscillatory behavior, which is driven by the dynamics of the middle part. This oscillatory behavior is due to the fact that the middle part is divided into two nearly synchronized clusters with different frequencies. Fig. 5b,c present the phase similarity matrix at two instances corresponding to the peak and trough of the fluctuations, as indicated by dashed lines in Fig. 5a. During the peak of fluctuations, the two clusters in the middle region come close to each other and almost synchronize. In contrast, at the trough, the clusters are spaced apart, with all nodes evenly distributed around the unit circle according to their frequencies. For a detailed look at the dynamics, the time evolutions of the order parameter and phase similarity matrix can be viewed in supplementary video, SV2.

To analyze the dynamics of the network in the second hysteresis loop, we plot the time evolution of the synchronization order parameter for the left, middle, and right parts (green, black, and red lines, respectively), along with the entire layer II (blue line) at an intralayer coupling of $\sigma = 2.11$ (see Fig. 6a). We observe that while the middle part is fully synchronized, the synchronization of the entire

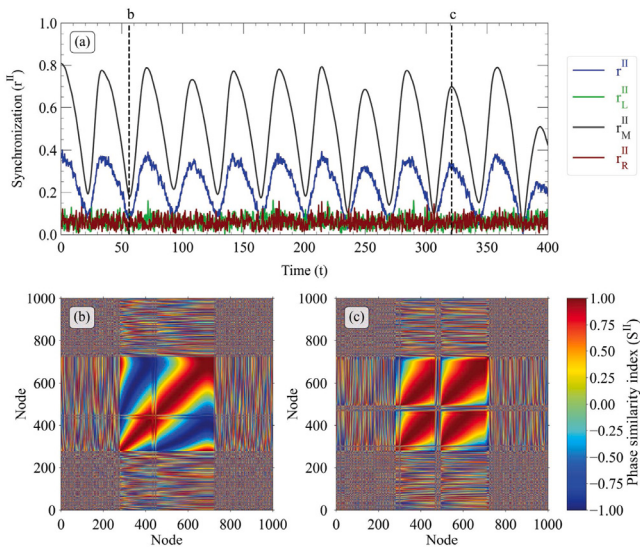


Fig. 5. A robust cyclic behavior in the order parameter is evident during the first hysteresis loop of the phase transition curve. (a) The evolution of the synchronization order parameter in the Regular frequency assignment model is illustrated by blue, green, black, and red curves, representing the entire layer and its left, middle, and right parts, respectively. (b) and (c) Two snapshots of the phase similarity matrix at the time instances indicated by the dashed lines in the top panel. The parameters are identical to those shown in Fig. 3d, with $\sigma = 0.39$.

layer exhibits periodic behavior influenced by the dynamics of the left and right sections.

The dynamics of the left and right sections clearly show that different waves with various frequencies are superimposed. Notably, low-frequency oscillations (LFOs) in the left and right parts are in-phase, while medium-frequency oscillations (MFOs) are in anti-phase, exhibiting a phase difference of π radians (see supplementary Fig. SF3 for better illustration). To gain clearer insight into these dynamics, we have created plots of the instantaneous phase similarity matrix at different time points (highlighted by dashed lines in Fig. 6b), from one peak to the next trough of the overall order parameter in the second and third rows. As previously mentioned, the middle part is synchronized for intralayer coupling beyond the first transition point, and we are now focusing on the second hysteresis loop. In the second and third rows, a red square in the center of each panel clearly indicates the synchronized middle part. Now, we will focus on the corners of the phase similarity matrices related to the dynamics of the left and right parts.

Fig. 6c,h display the phase similarity matrix at the time points when the entire layer (shown by the blue curve in Fig. 6a,b) reach its maximum and minimum oscillation. This illustrates the synchronization of the left and right parts with the middle part, as shown in Fig. 6c, indicating almost full synchronization ($r \approx 0.9$). In contrast, Fig. 6h shows the situation where the nodes on both sides are out of phase. Thus, the complete synchronization and the out-of-phase behavior of the corner parts correspond to the peaks and troughs associated with the LFOs observed in the waves of the entire layer, as well as in the left and right regions.

The phase similarity matrices in Fig. 6d-g depict the fluctuations between coherence and incoherence in the dynamics of the left and right parts during each LFO period. These panels illustrate how MFOs in the dynamics of the left and right parts — whose peaks are marked by dashed lines (c-f) in Fig. 6b — are superimposed on the low-frequency waves. Since the MFOs in the left and right parts are out of phase and effectively cancel each other out, they have no significant impact on the overall synchronization of the layer, as evidenced by the blue curve in Fig. 6a (refer to supplementary Fig. SF3 for a clearer illustration).

Fig. 6d,f display phase similarity matrices for the peaks of MFOs in the right part's dynamics (red curve in Fig. 6a,b), which correspond to

the troughs in the left part (green curve). In contrast, Fig. 6e,g present phase similarity matrices for the peaks (troughs) of MFOs in the left (right) part.

By analyzing the process through the backward curve shown in Fig. 6c-h, we can observe the following dynamics: initially, the entire layer is synchronized (see Fig. 6c). While the middle section remains synchronized, the outer parts of the left and right sections, which exhibit greater frequency differences between mirror nodes, unsynchronize and synchronize sequentially (Fig. 6d,e). This blinking process spreads throughout both sections, leading to fluctuations in their dynamics (Fig. 6f,g). Finally, during the trough of the overall wave, both sections are simultaneously out of phase (Fig. 6h). This procedure illustrates the dynamics of transitioning from a peak to a trough in the left or right parts. As it moves from the trough to the next peak, the process appears to reverse, shifting from Fig. 6h to Fig. 6c, and this pattern repeats in the following cycles (see the supplementary video, SV3 for a clear view of the blinking process).

As mentioned earlier, each layer forms a fully connected network of Kuramoto oscillators, with the same sets of natural frequencies. In the absence of the duplex arrangement of layers with frequency discrepancies and phase frustration ($\alpha = \frac{\pi}{2}$) in interlayer interactions, we would expect a continuous phase transition between incoherent and synchronized states within each layer. The distinctive phase transition observed, characterized by double hysteresis loops and intricate periodic behavior in each layer, directly results from the network's duplex architecture, especially the Regular frequency assignment model for the mirror nodes.

In Fig. 6i,j, we investigate the correlation between the dynamics of mirror nodes within this complex system. We achieve this by calculating the changes in phase similarities over time for each pair of mirror nodes, using the $S_{M_i}(t)$, for $i = 1 \dots N$, specifically focusing on intralayer coupling within the second hysteresis loop. Our results show that the mirror nodes in the middle part synchronize completely, while those on the left and right sides show periodic phase similarities. Fig. 6i illustrates this periodicity by plotting the oscillation frequency of the $S_{M_i}(t)$'s against the node number. The figure demonstrates that as the absolute value of frequency discrepancies between mirror nodes increases, the oscillation frequency in their phase similarity time series also rises. Thus, the periodic behavior observed in the evolution of the order parameter for both the left and right sections in each layer seems to be linked to the interactions between the layers, especially the complex dynamics of the mirror nodes within those sections.

As shown in Fig. 3d, the frequency differences between the counterpart mirror nodes in the left and right parts exhibit similar magnitudes but opposite signs ($\delta\omega_i = -\delta\omega_{(N+1-i)}$, for $i = 1, \dots, N$). This observation prompts an investigation into the potential relationship between the dynamics of the mirror nodes in the left and right sections. To explore this, we calculated the phase shift between the phase similarity time series of the counterpart mirror nodes (i.e., $S_{M_i}(t)$ and $S_{M_{N+1-i}}(t)$) and plotted the time average of the cosine of this phase shift against the node number, as shown in Fig. 6j. The phase of the time series $S_{M_i}(t)$, denoted as $\phi_i(t)$, is determined using the Hilbert transform by calculating the arctangent of the analytic signal. Since $\cos(\phi_i(t) - \phi_{N+1-i}(t)) = \cos(\phi_{N+1-i}(t) - \phi_i(t))$, this expression highlights the symmetry in the dynamics between the mirror pairs i and $N + 1 - i$. Consequently, a symmetric plot is observed around the center at $i = \frac{N}{2} = 500$ in Fig. 6j.

Each node in the middle part has a counterpart within the same part, whereas the counterparts of the nodes in the right part are found in the left part, and vice versa. As indicated in Fig. 6i, the nodes in the middle part are synchronized with each other and with their corresponding mirror nodes in the adjacent layer. Therefore, the counterpart mirror nodes associated with this part are correlated, as demonstrated by the values of 1 shown in Fig. 6j. In other words, for the intralayer coupling within the second hysteresis loop we are analyzing in Fig. 6, there is no information transfer occurring among the nodes in the middle sections of each layer, nor between those sections across different layers.

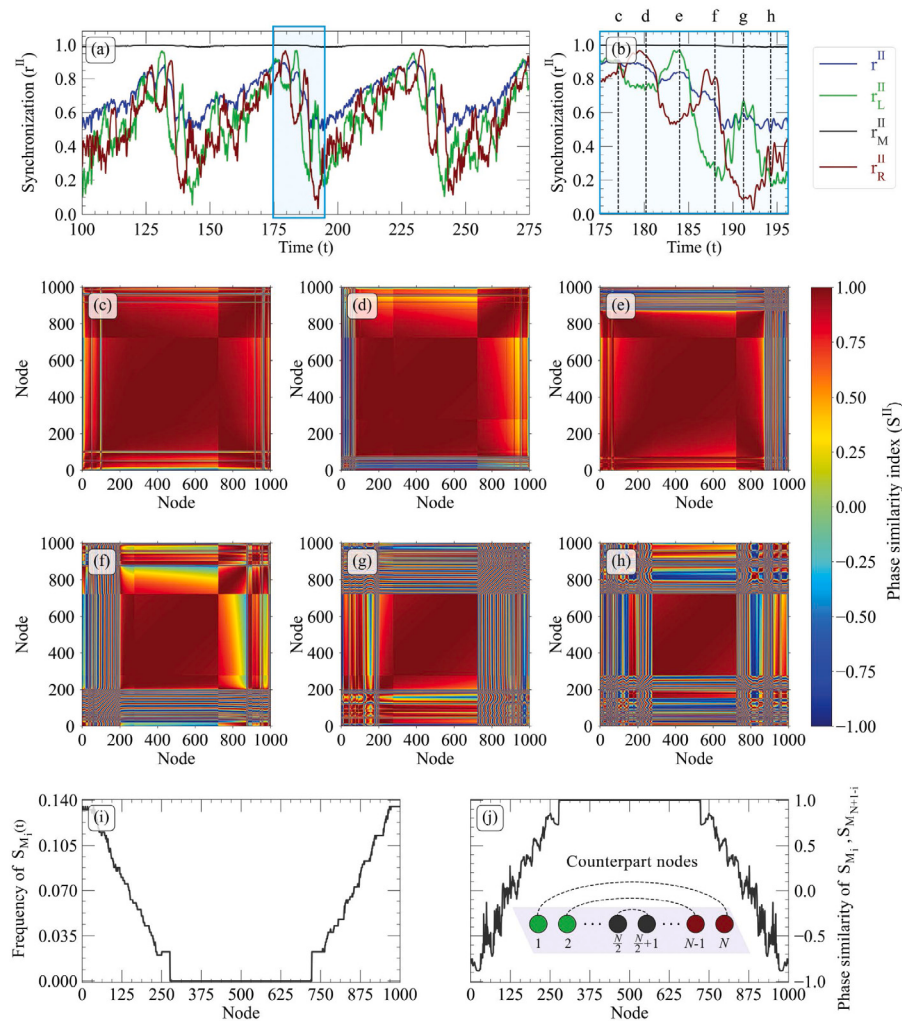


Fig. 6. Analyzing the intricate dynamics of each section of layer II in the second hysteresis loop of the phase transition curve. (a) Observing the evolution of the synchronization order parameter for the entire layer, as well as for the left, middle, and right parts, represented by the blue, green, black, and red lines, respectively. (b) A fragment of the panel a on an enlarged scale. (c-h) Six snapshots of the phase similarity matrix for the time points shown by the dashed lines in the panel (b). (i) Frequencies of phase similarities among mirror nodes. (j) Phase similarity of the counterparts' mirror nodes. The same parameters as those used in Fig. 3d were applied, utilizing a value of $\sigma = 2.11$.

As shown in Fig. 6i, the mirror nodes in the left and right parts are not phase-locked, exhibiting periodic phase similarities with an oscillation period related to the magnitude of their natural frequency differences. Furthermore, each pair of mirror nodes in the left (right) part has a counterpart pair in the right (left) part that shares the same magnitude of natural frequency differences but with opposite signs. Therefore, the phase similarity between the mirror nodes of both counterparts oscillates at similar frequencies, as illustrated in Fig. 6i; however, these oscillations are not in-phase.

Fig. 6j illustrates that the phase similarities time series of the two counterpart pairs are shifted according to the magnitude of their natural interlayer frequency differences. Indeed, for the counterpart node pairs with the greatest frequency differences from their corresponding mirror nodes, they are in anti-phase with each other, as indicated by the values of -1 in Fig. 6j. In other words, when the mirror nodes with the largest frequency differences in the right part are in-phase, their counterparts in the left part are in an anti-phase relation, and vice versa. The behavior of the counterpart mirror nodes increasingly resembles each other as their interlayer frequency differences decrease. This is particularly evident in the middle part, where the frequency difference between the mirror nodes in different layers is zero, resulting in identical behavior, as observed in Fig. 6i. The patterns observed in Fig. 6i,j do not appear in the intralayer couplings within the first hysteresis loop (see supplementary Fig. SF4). To observe how the phase

similarity between the i th pairs of mirror nodes $S_{M_i}(t)$ evolves over time and to understand the phase shift between the time series of counterpart mirror pairs $S_{M_i}(t)$ and $S_{M_{N+1-i}}(t)$ within each section, please refer to supplementary Fig. SF5.

The findings indicate that the superimposed waves and complex time-varying partial synchronization patterns observed in Fig. 6 arise from the information transfer between nodes in the right and left regions, both within and across each layer. It is important to note that while the mirror nodes may not be locked, the dynamics of the first layer are similar to those of the second layer (see supplementary Fig. SF6). In addition we observe that both layers are simultaneously synchronized, suggesting that interlayer synchronization is influenced early on, which can be attributed to the high interlayer coupling strength considered in our simulations (see supplementary Fig. SF7).

We noticed that the order parameter evolves over time, showing multiple oscillations at different frequencies, which are superimposed on each other. In other words, the system exhibits several oscillatory behaviors at distinct frequencies that occur simultaneously and overlap. Our goal is to explore the potential coupling between phase and amplitude within these oscillations. To achieve this, we employed the Fast Fourier Transform (FFT) to decompose the signals into three distinct frequency bands: LFOs ranging from 0.01 to 0.045 Hz, MFOs between 0.08 and 0.18 Hz, and HFOs spanning 0.5 to 3.5 Hz (refer to Fig. 7a,b). Applying the Hilbert transform to each signal in various frequency

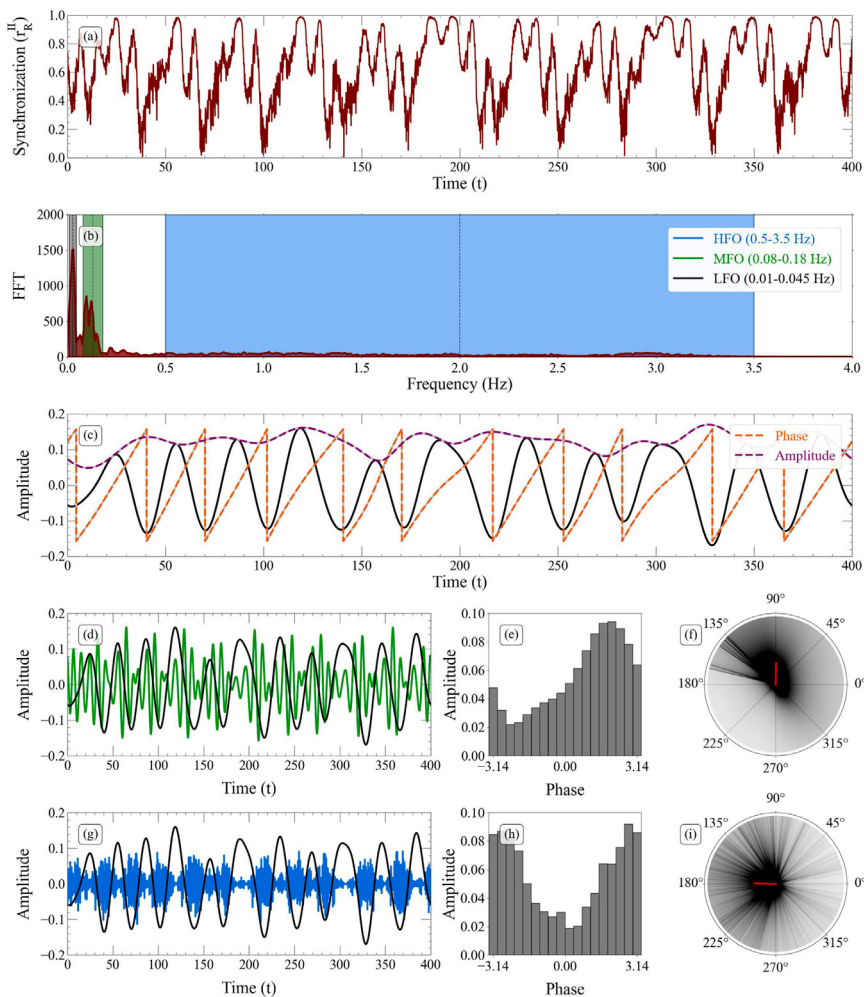


Fig. 7. Analysis of phase–amplitude coupling (PAC) among distinct frequency bands of oscillations. (a) The simulated signal displays the synchronization order parameter for the right part in layer II over time, utilizing parameters from Fig. 3d, with, $\sigma = 2.29$, within the second hysteresis loop. (b) FFT visualization with color-coding for low (LFO), medium (MFO), and high (HFO) frequency oscillations. (c) The black line represents the inverse Fourier transform of the LFOs, with the orange and purple dashed lines indicating its phase and amplitude. (d-f) PAC between LFOs and MFOs, measured using (e) PLV and (f) MVL modulation indices. (g-i) Comparable calculations for LFOs and HFOs.

bands allows us to find the phase and amplitude at each time point. Fig. 7c displays the LFOs extracted from the right part order parameter (black line), along with its phase (orange dashed line) and amplitude (purple dashed line). The fourth and fifth rows display the PAC between LFOs and MFOs, and between LFOs and HFOs, respectively. Fig. 7d shows the LFOs and MFOs signals and Fig. 7g shows the LFOs and HFOs signals. To visualize the interactions, the average amplitudes of MFOs and HFOs are plotted against the LFOs phase in Fig. 7e,h.

Fig. 7f,i illustrate phase clustering biases in polar space. Investigations confirm a clear connection between LFO phase and MFO and HFO amplitudes: MFO peaks at LFO phase $\frac{\pi}{2}$ and HFO peaks at π . The PLV for MFOs and HFOs is 0.315 and 0.307, respectively. Similarly, the MVL is 0.032 and 0.038, respectively. Comparable results are obtained using the signal from the right part.

So far, we have explored how the Regular arrangement of mirror node frequencies affects the dynamics of a duplex network with interlayer coupling set at $\lambda = 10$, an average frequency difference of $\Delta\omega = 0.8$, and interlayer frustration fixed at $\alpha = \frac{\pi}{2}$. Our findings showed two hysteresis loops in the transition curves, indicating complex dynamics. The rows of Fig. 8 depict how these transition curves evolve in response to changes in the parameters λ , $\Delta\omega$, and α , respectively. The first column shows the transition curve for different parameter values along the backward path. The blue shades, which range from light to dark, illustrate the transition diagrams for the parameter under study as it progresses from lower to higher levels. Meanwhile, the second column

emphasizes the locations of the first jumps (green circles) and the second jumps (red triangles) in the transition curves in relation to the parameter values.

The blue shades in Fig. 8a, ranging from light to dark, illustrate the transition diagrams for interlayer coupling levels as they progress from lower to higher values. In Fig. 8b, it is evident that with increasing interlayer coupling, the first and second transitions take place at higher intralayer coupling parameter values. As a result, the rise in the interlayer coupling coefficient postpones the transitions and leads to sharper transitions, emphasizing that the duplex structure of the network contributes to these atypical transitions.

In Fig. 8c,d, we examine how average mirror node frequencies affect the phase transition. Small $\Delta\omega$ values create a more pronounced initial transition at lower intralayer coupling due to our model, which allocates more nodes to the middle section. A larger synchronized middle section leads to greater jumps during the first transition. Meanwhile, the smaller corner sections, which have a larger frequency difference, are less likely to disrupt the synchronization of the middle section. This facilitates synchronization in the middle section, resulting in a smaller transition point with a lower $\Delta\omega$. Additionally, smaller values of $\Delta\omega$, resulting from the smaller sizes of the corner sections, lead to a decrease in the height of the second transition jumps associated with their synchronization.

The earlier study indicated that frustration near $\frac{\pi}{2}$ leads to hysteresis loops [31]. In Fig. 8e,f, we found that increasing frustration around

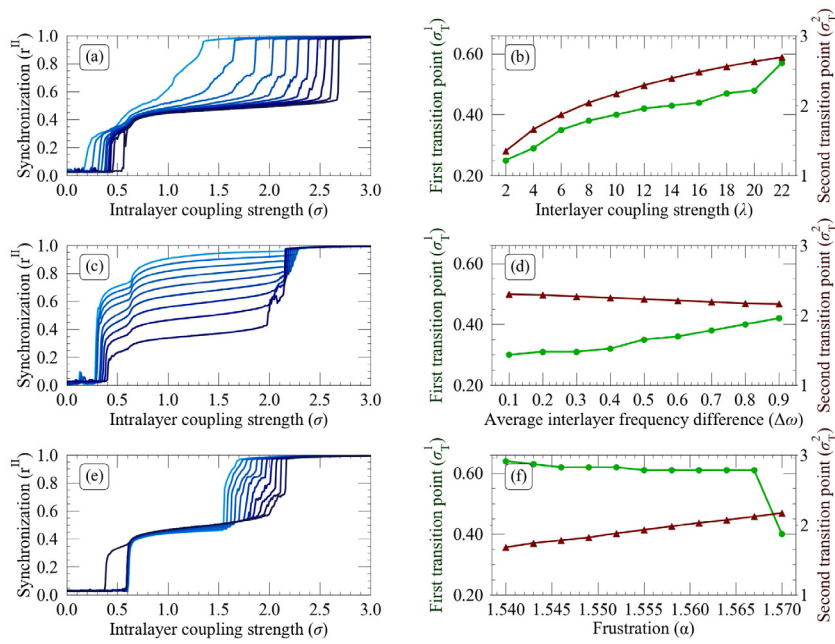


Fig. 8. Analysis of phase transition modifications resulting from parameter variations in the Regular model along the backward path. Each row examines the effect of modifying a single network parameter while keeping the others constant. (a, b) Variation of interlayer coupling (λ), with fixed $\alpha = \frac{\pi}{2}$ and $\Delta\omega = 0.8$. (c, d) Variation of the average natural frequency difference ($\Delta\omega$), with fixed $\lambda = 10$ and $\alpha = \frac{\pi}{2}$. (e, f) Variation of the frustration parameter (α), with fixed $\lambda = 10$ and $\Delta\omega = 0.8$. (a, c, e) Presents the synchronization phase transition as a function of intralayer coupling, while (b, d, f) highlights the critical intralayer coupling values corresponding to the first (green circle) and second (red triangle) jumps. The phase transition curves shift from light to dark blue, representing low to high values of the examined parameters.

$\frac{\pi}{2}$ decreases the first transition points while increasing the second ones. The effect of frustration change is more pronounced during the second transition, which involves the synchronization of the left and right sections. This is because these sections exhibit greater frequency differences between mirror nodes. In fact, as frustration approaches $\frac{\pi}{2}$, it becomes increasingly difficult for the left and right sections to synchronize with the entire network.

3. Discussion

This study intricately investigates the dynamics of duplex networks, emphasizing the significance of frequency distributions among mirror nodes in shaping phase transitions and synchronization across network layers. Building upon earlier findings that underscored the potential for explosive synchronization due to frequency mismatches between network layers and the inclusion of $\frac{\pi}{2}$ frustration within interlayer connections in duplex networks [31], our study contributes novel insights to this domain.

Expanding on the work by Kumar et al. [31], our research advances understanding by not only highlighting the pivotal role of average frequency differences between mirror nodes in phase transitions but also emphasizing the critical influence of the specific configuration of these frequencies on transition dynamics. We introduce a Regular frequency assignment model where each layer comprises consistent arrays of natural frequencies evenly distributed between -0.5 and 0.5. Nodes in each layer are classified into three groups: left, middle, and right, with mirror nodes in these groups displaying positive, neutral, and negative frequency differences ($\delta\omega_i$, for $i = 1, \dots, N$), respectively. By manipulating the sizes of these groups, we can control the average frequency differences and compare the behavior of this model with a Randomly frequency assignment model featuring equivalent average frequency discrepancies.

Our preliminary findings are in line with the outcomes presented by Kumar et al. [31], demonstrating that random frequency differences among mirror nodes induce explosive synchronization when $\alpha = \frac{\pi}{2}$. Conversely, this phenomenon leads to a continuous phase transition when $\alpha = 0$.

Our research uncovers that in the Regular frequency assignment model, a hysteresis loop emerges on the transition curve even when $\alpha = 0$, indicating abrupt synchronization of nodes with $\delta\omega_i \neq 0$ in the peripheral sections, contrasting the gradual phase transition observed in the Random model at $\alpha = 0$. This should be due to the multimodal distribution of frequency discrepancies.

Previous studies have examined the impact of natural frequency distributions on single-layer networks. Martens et al. investigated globally connected networks with bimodal frequency distributions, uncovering states such as incoherence, partial synchrony, and standing waves with anti-phase groups, while highlighting memory and irreversibility in transition curves [47]. In contrast, our study focuses on two globally connected layers with uniform frequency distributions. When merged into a duplex network using the Regular frequency assignment model, we observed irreversible traits in the phase transition curves that arise solely from the unique frequency allocation in the duplex structure.

In the Regular frequency arrangement model with $\alpha = 0$, abrupt synchronization occurs among peripheral nodes, distinguished by frequency differentials from their mirrored pairs, followed by reversible synchronization in the middle section, where node frequencies align precisely with their mirrored pairs. At $\alpha = \frac{\pi}{2}$, we observe double hysteresis loops. Unlike $\alpha = 0$, at low intralayer couplings, the middle nodes are synchronized, while at higher couplings, the peripheral nodes achieve synchronization. In fact, frustration alters the synchronization order: with zero frustration, peripheral sections synchronize first, followed by the central section as intralayer coupling increases; this order is reversed at $\alpha = \frac{\pi}{2}$. We should note that, unlike the Random frequency assignment model, in the Regular model, when $\alpha = \frac{\pi}{2}$, there is also an abrupt transition observed for nodes with zero frequency discrepancies from their mirrored pairs. An earlier study explored consecutive explosive transitions in multilayer networks, focusing on the interaction between a dynamical layer of phase oscillators and an approximately synchronized environmental layer. However, unlike our study, their analysis examined phase transitions by varying the interlayer coupling without considering the frequency discrepancy distribution [50].

The double hysteresis loop in our model is not caused by the specific frequency arrangement in the second layer but rather by the

shape of the distribution function of frequency differences between mirror nodes. Specifically, the standard deviation and modality of this distribution determine the nature of phase synchronization and the number of hysteresis loops. Kumar et al. reported a continuous phase transition for a Random model with zero average frequency differences between mirror nodes (where each pair of mirror nodes has equal frequencies) [31]. In this case, the distribution function of frequency differences is a Dirac delta function with zero mean and zero standard deviation. We argue that their observed continuous phase transition is a direct consequence of the zero standard deviation in the frequency difference distribution.

In our work, we demonstrate that variability in frequency differences around their mean triggers an explosive phase transition in duplex networks with frustrated interlayer interactions, even when the mean frequency differences are zero (see supplementary Fig. SF8). Furthermore, in the Regular model, the multimodal distribution of frequency differences leads to dynamic clusters and double hysteresis loops, whereas the Random model's nearly uniform and unimodal distribution results in an explosive transition with a single hysteresis loop (see Figs. 2 and 3).

The detailed examination of the instantaneous phase similarity matrices for intralayer coupling across both hysteresis loops shows a periodic pattern in the synchronization of each layer. In the first hysteresis loop, at low intralayer couplings, this periodicity originates from the synchronization of the middle section. In contrast, in the second hysteresis loop, the synchronization order parameter for the left and right sections behaves periodically.

The periodic behavior observed in the initial hysteresis loops is straightforward and connected to the formation of synchronized groups with varying frequencies among the nodes in the middle section. In contrast, the periodic behavior observed in the second hysteresis loops — related to the synchronization of the left and right sections — displays a complex wave composed of multiple frequencies. This complexity arises from the intricate interactions between the left and right sections, both within and across layers. Throughout this process, the synchronization of nodes in each left and right section shifts between coherent and incoherent states across different time scales, a phenomenon we refer to as the blinking process. Furthermore, our findings indicate that the overlapping waves are not independent; rather, the amplitudes of the higher frequency oscillatory components are selectively amplified at specific phases of the lower-frequency signal.

In nature, many waveforms are complex and composed of multiple frequencies. Thus, exploring the structures that contribute to these synchronization patterns is intriguing. For instance, periodic signals in Electroencephalography (EEG) represent essential neural synchronization patterns vital for understanding brain states and cognitive functions. Additionally, these oscillations are not independent; they clearly exhibit signs of interaction [62,68,69]. For example, gamma activity has been shown to couple with opposing theta phases during both encoding and recall memory processes, as evidenced by local field potentials [70].

In conclusion, our study highlights the essential connection between frequency distribution and network dynamics in two-layer systems. Given that many real-world networks, including those in the brain, are multilayered and consist of heterogeneous entities with varying firing frequencies, our findings provide a vital framework for further exploration of these complex systems. For example, various complex behaviors observed in networks, such as phase-amplitude coupling, may arise from the interplay between frequency distribution, phase lag, and multilayer interactions. We emphasize the necessity for ongoing research in this area to deepen our understanding of these intricate dynamics.

CRediT authorship contribution statement

Ali Seif: Writing – original draft, Visualization, Validation, Software, Investigation, Formal analysis. **Mina Zarei:** Writing – review & editing, Writing – original draft, Supervision, Project administration, Methodology, Investigation, Conceptualization.

Declaration of competing interest

The authors declare that there are no competing interests related to this work.

Appendix A. Supplementary data

Supplementary material related to this article can be found online at <https://doi.org/10.1016/j.chaos.2025.116412>.

Data availability

The datasets generated and analyzed during the current study are available in the Github repository, <https://github.com/Articles-data/Frequency-Arrangement>.

References

- [1] Shahal Shir, et al. Synchronization of complex human networks. *Nat Commun* 2020;11. <http://dx.doi.org/10.1038/s41467-020-17540-7>.
- [2] Bianconi Ginestra. Multilayer networks: structure and function. Oxford; 2018, <http://dx.doi.org/10.1093/oso/9780198753919.001.0001>.
- [3] Kivelä Mikko, et al. Multilayer networks. *J Complex Netw* 2014;2. <http://dx.doi.org/10.1093/comnet/cnu016>.
- [4] Boccaletti Stefano, et al. The structure and dynamics of multilayer networks. *Phys Rep* 2014;544. <http://dx.doi.org/10.1016/j.physrep.2014.07.001>.
- [5] De Domenico Manlio, et al. Mathematical formulation of multilayer networks. *Phys Rev X* 2013;3. <http://dx.doi.org/10.1103/PhysRevX.3.041022>.
- [6] Danziger Michael M, et al. Dynamic interdependence and competition in multilayer networks. *Nat Phys* 2019;15. <http://dx.doi.org/10.1038/s41567-018-0343-1>.
- [7] Vaiana Michael, Muldoon Sarah Feldt. Multilayer brain networks. *J Nonlinear Sci* 2020;30. <http://dx.doi.org/10.1007/s00332-017-9436-8>.
- [8] Lim Sol, et al. Discordant attributes of structural and functional brain connectivity in a two-layer multiplex network. *Sci Rep* 2019;9. <http://dx.doi.org/10.1038/s41598-019-39243-w>.
- [9] Battiston Federico, et al. Multilayer motif analysis of brain networks. *Chaos: An Interdiscip J Nonlinear Sci* 2017;27. <http://dx.doi.org/10.1063/1.4979282>.
- [10] Bentley Barry, et al. The multilayer connectome of *Caenorhabditis elegans*. *PLoS Comput Biol* 2016;12. <http://dx.doi.org/10.1371/journal.pcbi.1005283>.
- [11] Buldú Javier M, Porter Mason A. Frequency-based brain networks: From a multiplex framework to a full multilayer description. *Netw Neurosci* 2018;2. <http://dx.doi.org/10.1162/netn-a-00033>.
- [12] De Domenico Manlio, Sasai Shuntaro, Arenas Alex. Mapping multiplex hubs in human functional brain networks. *Front Neurosci* 2016;10. <http://dx.doi.org/10.3389/fnins.2016.00326>.
- [13] Strogatz Steven. Sync: The emerging science of spontaneous order. 2003, Penguin UK. <https://www.stevenstrogatz.com/books/sync-the-emerging-science-of-spontaneous-order>.
- [14] Tang Yang, et al. Synchronization in complex networks and its application—a survey of recent advances and challenges. *Annu Rev Control* 2014;38. <http://dx.doi.org/10.1016/j.arcontrol.2014.09.003>.
- [15] Arenas Alex, et al. Synchronization in complex networks. *Phys Rep* 2008;469. <http://dx.doi.org/10.1016/j.physrep.2008.09.002>.
- [16] Smeal Roy M, Bard Ermentrout G, White John A. Phase-response curves and synchronized neural networks. *Philos Trans R Soc B: Biol Sci* 2010;365. <http://dx.doi.org/10.1098/rstb.2009.0292>.
- [17] Stiefel Klaus M, Bard Ermentrout G. Neurons as oscillators. *J Neurophysiol* 2016;116. <http://dx.doi.org/10.1152/jn.00525.2015>.
- [18] Börgers Christoph. An introduction to modeling neuronal dynamics, vol. 66. Springer; 2017, <http://dx.doi.org/10.1007/978-3-319-51171-9>.
- [19] Kuramoto Y. Chemical turbulence: chemical oscillations, waves, and turbulence, vol. 19, Springer; 1984, <http://dx.doi.org/10.1007/978-3-642-69689-3>.
- [20] Yeung MK Stephen, Strogatz Steven H. Time delay in the Kuramoto model of coupled oscillators. *Phys Rev Lett* 1999;82. <http://dx.doi.org/10.1103/PhysRevLett.82.648>.
- [21] Ziaeemehr Abolfazl, et al. Frequency-dependent organization of the brain's functional network through delayed-interactions. *Neural Netw* 2020;132. <http://dx.doi.org/10.1016/j.neunet.2020.08.003>.
- [22] Filatrella Giovanni, Nielsen Arne Hejde, Pedersen Niels Falsig. Analysis of a power grid using a Kuramoto-like model. *Eur Phys J B* 2008;61. <http://dx.doi.org/10.1140/epjb/e2008-00098-8>.
- [23] Mahdavi Esmaeil, Zarei Mina, Shahbazi Farhad. Synchronization of two coupled phase oscillators in the time-delayed second-order Kuramoto model. 2024, Preprint at <https://arxiv.org/abs/2406.01208>.

- [24] JSakaguchi Hidetsugu, Kuramoto Yoshiaki. A soluble active rotator model showing phase transitions via mutual entrainment. *Progr Theoret Phys* 1986;76. <http://dx.doi.org/10.1143/PTP.76.576>.
- [25] Sakaguchi Hidetsugu, Shinomoto Shigeru, Kuramoto Yoshiaki. Mutual entrainment in oscillator lattices with nonvariational type interaction. *Progr Theoret Phys* 1988;79. <http://dx.doi.org/10.1143/PTP.79.1069>.
- [26] Mahdavi Esmaili, Zarei Mina, Shahbazi Farhad. Synchronization of frustrated phase oscillators in the small-world networks. *Eur Phys J Plus* 2022;137. <http://dx.doi.org/10.1140/epjp/s13360-022-03096-6>.
- [27] Nicosia Vincenzo, et al. Collective phenomena emerging from the interactions between dynamical processes in multiplex networks. *Phys Rev Lett* 2017;118. <http://dx.doi.org/10.1103/PhysRevLett.118.138302>.
- [28] Zhang Xiyun, et al. Explosive synchronization in adaptive and multilayer networks. *Phys Rev Lett* 2015;114. <http://dx.doi.org/10.1103/PhysRevLett.114.038701>.
- [29] Jalan Sarika, Kumar Anil, Leyva Inmaculada. Explosive synchronization in frequency displaced multiplex networks. *Chaos* 2019;29. <http://dx.doi.org/10.1063/1.5092226>.
- [30] Jalan Sarika, et al. Inhibition-induced explosive synchronization in multiplex networks. *Phys Rev E* 2019;99. <http://dx.doi.org/10.1103/PhysRevE.99.062305>.
- [31] Kumar Anil, Jalan Sarika. Explosive synchronization in interlayer phase-shifted Kuramoto oscillators on multiplex networks. *Chaos: An Interdiscip J Nonlinear Sci* 2021;31. <http://dx.doi.org/10.1063/5.0043775>.
- [32] Kachhvah Ajay Deep, Jalan Sarika. Delay regulated explosive synchronization in multiplex networks. *New J Phys* 2019;21. <http://dx.doi.org/10.1088/1367-2630/aaff0e>.
- [33] Kumar Anil, Jalan Sarika, Kachhvah Ajay Deep. Interlayer adaptation-induced explosive synchronization in multiplex networks. *Phys Rev Res* 2020;2. <http://dx.doi.org/10.1103/PhysRevResearch.2.023259>.
- [34] Jain Priya B, et al. Composed solutions of synchronized patterns in multiplex networks of Kuramoto oscillators. *Chaos: An Interdiscip J Nonlinear Sci* 2023;33. <http://dx.doi.org/10.1063/5.0161399>.
- [35] Rathore Vasundhara, Suman Ayushi, Jalan Sarika. Synchronization onset for contrarians with higher-order interactions in multilayer systems. *Chaos: An Interdiscip J Nonlinear Sci* 2023;33. <http://dx.doi.org/10.1063/5.0166627>.
- [36] Skardal Per Sebastian, Arenas Alex. Higher order interactions in complex networks of phase oscillators promote abrupt synchronization switching. *Commun Phys* 2020;3. <http://dx.doi.org/10.1038/s42005-020-00485-0>.
- [37] Sadilek Maximilian, Thurner Stefan. Physiologically motivated multiplex Kuramoto model describes phase diagram of cortical activity. *Sci Rep* 2015;5. <http://dx.doi.org/10.1038/srep10015>.
- [38] Buldyrev Sergey V, et al. Catastrophic cascade of failures in interdependent networks. *Nature* 2010;464. <http://dx.doi.org/10.1038/nature08932>.
- [39] Kumar Pawan, et al. Experimental evidence of explosive synchronization in mercury beating-heart oscillators. *Phys Rev E* 2015;91. <http://dx.doi.org/10.1103/PhysRevE.91.062909>.
- [40] Lee UnCheol, et al. Functional brain network mechanism of hypersensitivity in chronic pain. *Sci Rep* 2018;8. <http://dx.doi.org/10.1038/s41598-017-18657-4>.
- [41] Adhikari Bhim M, Epstein Charles M, Dhamala Mukesh. Localizing epileptic seizure onsets with Granger causality. *Phys Rev E— Stat Nonlinear, Soft Matter Phys* 2013;88. <http://dx.doi.org/10.1103/PhysRevE.88.030701>.
- [42] Boccaletti S, et al. Explosive transitions in complex networks' structure and dynamics: Percolation and synchronization. *Phys Rep* 2016;660. <http://dx.doi.org/10.1016/j.physrep.2016.10.004>.
- [43] Zhang Xiyun, et al. Explosive synchronization in a general complex network. *Phys Rev E* 2013;88. <http://dx.doi.org/10.1103/PhysRevE.88.010802>.
- [44] D'Souza Raissa M, et al. Explosive phenomena in complex networks. *Adv Phys* 2019;68. <http://dx.doi.org/10.1080/00018732.2019.1650450>.
- [45] Gómez-Gardenes Jesús, et al. Explosive synchronization transitions in scale-free networks. *Phys Rev Lett* 2011;106. <http://dx.doi.org/10.1103/PhysRevLett.106.128701>.
- [46] Papadopoulos Lia, et al. Development of structural correlations and synchronization from adaptive rewiring in networks of Kuramoto oscillators. *Chaos: An Interdiscip J Nonlinear Sci* 2017;27. <http://dx.doi.org/10.1063/1.4994819>.
- [47] Martens Erik Andreas, et al. Exact results for the Kuramoto model with a bimodal frequency distribution. *Phys Rev E— Stat Nonlinear, Soft Matter Phys* 2009;79. <http://dx.doi.org/10.1103/PhysRevE.79.026204>.
- [48] Khanra Pitambar, et al. Explosive synchronization in phase-frustrated multiplex networks. *Phys Rev E* 2018;98. <http://dx.doi.org/10.1103/PhysRevE.98.052315>.
- [49] Soriano-Paños David, et al. Explosive transitions induced by interdependent contagion-consensus dynamics in multiplex networks. *Phys Rev E* 2019;99. <http://dx.doi.org/10.1103/PhysRevE.99.062311>.
- [50] Wu Tianwei, et al. Double explosive transition in the synchronization of multilayer networks. *Phys Rev Res* 2022;4. <http://dx.doi.org/10.1103/PhysRevResearch.4.033009>.
- [51] Jalan Sarika, Kachhvah Ajay Deep, Jeong Hawoong. Explosive synchronization in multilayer dynamically dissimilar networks. *J Comput Sci* 2020;46. <http://dx.doi.org/10.1016/j.jocs.2020.101177>.
- [52] Kachhvah Ajay Deep, Jalan Sarika. Explosive synchronization and chimera in interpinned multilayer networks. *Phys Rev E* 2021;104. <http://dx.doi.org/10.1103/PhysRevE.104.L042301>.
- [53] Kachhvah Ajay Deep, et al. Interlayer Hebbian plasticity induces first-order transition in multiplex networks. *New J Phys* 2020;22. <http://dx.doi.org/10.1088/1367-2630/abcf6b>.
- [54] Ziaeemehr Abolfazl, Zarei Mina, Sheshbolouki Aida. Emergence of global synchronization in directed excitatory networks of type I neurons. *Sci Rep* 2020;10. <http://dx.doi.org/10.1038/s41598-020-60205-0>.
- [55] Skardal Per Sebastian, et al. Erosion of synchronization in networks of coupled oscillators. *Phys Rev E* 2015;91. <http://dx.doi.org/10.1103/PhysRevE.91.010802>.
- [56] Breden Markus, Kalloniatis Alexander C. Frustration tuning and perfect phase synchronization in the Kuramoto-Sakaguchi model. *Phys Rev E* 2016;93. <http://dx.doi.org/10.1103/PhysRevE.93.062315>.
- [57] Xu Tianle, et al. Maximal hysteretic range for explosive synchronization. *Chaos Solitons Fractals* 2024;180. <http://dx.doi.org/10.1016/j.chaos.2024.114455>.
- [58] Seymour Robert A, Rippon Gina, Kessler Klaus. The detection of phase amplitude coupling during sensory processing. *Front Neurosci* 2017;11. <http://dx.doi.org/10.3389/fnins.2017.00487>.
- [59] Daume Jonathan, et al. Phase-amplitude coupling and long-range phase synchronization reveal frontotemporal interactions during visual working memory. *J Neurosci* 2017;37. <http://dx.doi.org/10.1523/JNEUROSCI.2130-16.2016>.
- [60] Lega Bradley, et al. Slow-theta-to-gamma phase-amplitude coupling in human hippocampus supports the formation of new episodic memories. *Cerebral Cortex* 2016;26. <http://dx.doi.org/10.1093/cercor/bhu232>.
- [61] Vanhatalo Sampska, et al. Infraslow oscillations modulate excitability and interictal epileptic activity in the human cortex during sleep. *Proc Natl Acad Sci* 2004;101. <http://dx.doi.org/10.1073/pnas.0305375101>.
- [62] Tort Adriano BL, et al. Measuring phase-amplitude coupling between neuronal oscillations of different frequencies. *J Neurophysiol* 2010;104. <http://dx.doi.org/10.1152/jn.00106.2010>.
- [63] Cohen Michael X, Elger Christian E, Fell Juergen. Oscillatory activity and phase-amplitude coupling in the human medial frontal cortex during decision making. *J Cogn Neurosci* 2008;21. <http://dx.doi.org/10.1162/jocn.2008.212020>.
- [64] Combrisson Etienne, et al. Tensorpac: An open-source Python toolbox for tensor-based phase-amplitude coupling measurement in electrophysiological brain signals. *PLoS Comput Biol* 2020;16. <http://dx.doi.org/10.1371/journal.pcbi.1008302>.
- [65] Hülsemann Mareike J, Naumann Ewald, Rasch Björn. Quantification of phase-amplitude coupling in neuronal oscillations: comparison of phase-locking value, mean vector length, modulation index, and generalized-linear-modeling-cross-frequency-coupling. *Front Neurosci* 2019;13. <http://dx.doi.org/10.3389/fnins.2019.00573>.
- [66] Lachaux Jean-Philippe, et al. Measuring phase synchrony in brain signals. *Hum Brain Mapp* 1999;8. [http://dx.doi.org/10.1002/\(SICI\)1097-0193\(1999\)8:4<194::AID-HBM4>3.0.CO;2-C](http://dx.doi.org/10.1002/(SICI)1097-0193(1999)8:4<194::AID-HBM4>3.0.CO;2-C).
- [67] Canolty Ryan T, et al. High gamma power is phase-locked to theta oscillations in human neocortex. *Science* 2006;313. <http://dx.doi.org/10.1126/science.1128115>.
- [68] Hanslmayr Simon, Staudigl Tobias. How brain oscillations form memories—a processing based perspective on oscillatory subsequent memory effects. *Neuroimage* 2014;85. <http://dx.doi.org/10.1016/j.neuroimage2013.05.121>.
- [69] Voytek Bradley, et al. Shifts in gamma phase-amplitude coupling frequency from theta to alpha over posterior cortex during visual tasks. *Front Hum Neurosci* 2010;4. <http://dx.doi.org/10.3389/fnhum.2010.00191>.
- [70] Saint Amour di Chanaz Ludovico, et al. Gamma amplitude is coupled to opposed hippocampal theta-phase states during the encoding and retrieval of episodic memories in humans. *Curr Biol* 2023;33. <http://dx.doi.org/10.1016/j.cub.2023.03.073>.